Selection of Aluminium and its Alloys for Aluminium–Air Batteries Using Pourbaix Diagrams and Finite Element Modelling

S. R. Dhanushkodi[1, *], S. Sangeetha[2], M. N. Babu[3] and M. W. Fowler[4]

[1]*Dhanushkodi Research Group, Department of Chemical Engineering, Vellore Institute of Technology, Katpadi, Vellore, India*
[2]*Department of Electronics Engineering, College of Engineering, Guindy, Anna University, Chennai, India*
[3]*Metallurgy and Material Group, Indira Gandhi Center for Atomic Energy, Kalpakkam, India*
[4]*Department of Chemical Engineering, University of Waterloo, Waterloo, Canada*
*Corresponding author. E-mail address: *shankarraman.d@vit.ac.in*

Received 10/07/2025; accepted 10/12/2025
https://doi.org/10.4152/pea.2027450508

Abstract
The development of aluminum–air batteries provide a promising solution for stabilizing intermittent renewable energy sources, such as solar and wind. A significant challenge to their large-scale deployment is the stability on aluminum electrodes in the electrolyte, which presents both economic and corrosion-related challenges. Issues related to corrosion, cost and electrode thinning compromises the performance of aluminum electrodes. Nonetheless, aluminum alloys are emerging as a compelling alternative for aluminium electrodes due to their high electrochemical activity and ease of processing. Herein, an integrated framework that combines Pourbaix diagrams (PD) with finite element modeling (FEM) is proposed to systematically investigate the stability of aluminum-based electrode materials. Within this framework, PD predict the stability regions of key electro active species of aluminum and its alloys, such as Al $(OH)_3$, AlO_2^- and Al $(OH)_4^-$, under various pH, concentration and temperature. PD offer a comprehensive assessment of material behavior in corrosive environments. A FEM model incorporated in the framework illustrates thinning of the electrode–electrolyte interface due to electrode corrosion. The model predictions are validated against experimental data in an inbuilt cell, showing good agreement in electrode thickness reduction and corrosion rate predictions under acidic conditions. The model shows that pure Al obtained a pit with a depth of 1.31 mm at overpotential of 1.93 V, while Al 7075 eroded into a 1.9 mm pit at 1.87 V, thus having a larger corroded area. These findings provide a foundation for screening aluminum-based electrodes based on corrosion rates and thermodynamics parameters for batteries used in energy storage systems.

Keywords: Pourbaix diagram; passivation; Finite element model; Tafel polarization curve.

Introduction•

The advancement of high-performance energy storage systems is essential for implementing sustainable energy infrastructures. As the demand for efficient storage

•The abbreviations list is in page 473.

solutions increases, aluminum-air (Al-air) batteries have emerged as a promising technology due to their high theoretical gravimetric energy density, economic viability and the abundant availability of this element. These batteries capitalize on aluminum's high capacity and utilization of atmospheric oxygen as cathodic reactant, offering a lightweight design and theoretical energy densities exceeding 8 kWh/kg^{-1}, thereby presenting themselves as attractive alternatives to conventional lithium-ion chemistries. Their potential to facilitate large-scale, low-cost energy storage solutions, particularly for grid storage and off-grid applications, positions them as a suitable technology to complement intermittent renewable energy sources such as solar and wind. Among key advantages of Al–air batteries are their use of environmentally benign and widely available materials, including aluminum and electrolytes like potassium hydroxide or ionic liquids. These materials are preferred due to their high ionic conductivity, solubility and compatibility with sustainable energy goals [1-3]. A critical aspect in the advancement of this technology is the complex interaction between electrodes and electrolytes across various pH levels of the electrolyte. This interaction can result in undesirable electrochemical reactions and an elevated corrosion rate at the electrode surface under different concentrations and temperature of the battery cells. The passive oxide films would be formed at the interface between aluminum and electrolyte. These films substantially hinder electron transfer and ion movement necessary for anodic dissolution, which drives battery discharge [3-6]. The stability of these oxide films primarily composed of Al_2O_3 and Al (OH) is heavily dependent on the electrolyte's pH of and the electrode potential. Both electrochemical activity and solubility of aluminum are highly pH-dependent, which in turn influences battery performance and durability.

Pourbaix diagrams (PD), which map thermodynamic parameters of species as a function of electrochemical potential, are vital tools for evaluating redox behavior of aluminum-based electrode materials [7-10]. They play a key role in predicting corrosion potentials, selecting the design of stable electrolytes, assessing electrode layers and optimizing electrode-electrolyte interfaces to improve the battery lifespan. Consequently, PD are essential for understanding and mitigating electrode corrosion in operating batteries. PD map thermodynamic stability of aluminum species based on pH and electrode potential, illustrating the narrow range in which the passive oxide film remains stable [11-13]. Outside this range, aluminum either corrodes actively by forming aluminate complexes or degrades rapidly due to hydrogen evolution reactions. Table 1 and 2 present E_{corr} reported for different conditions in literature [13-29]. This insight is crucial for determining performance limits of aluminum in different electrolytes, and for developing novel strategies to enhance electrode design and battery efficiency.

Alkaline electrolytes perform a dual function in dissolution of aluminum by disrupting the oxide film while simultaneously facilitating hydrogen evolution, which adversely

affects coulombic efficiency and accelerates anode degradation. Consequently, the design of optimal electrodes necessitates a careful balance of these competing factors to enhance energy efficiency. At the nanoscale, interfacial chemistry of aluminum becomes increasingly complex, primarily due to the bilayer structure of the oxide film, which comprises a dense inner layer and a hydrated, porous outer layer. Variation in microstructure and defect chemistry within these oxide layers is pivotal in governing charge transfer, thereby influencing progression of pitting corrosion. To address these challenges, literature proposes alloying aluminum with elements such as gallium, tin and indium for the batteries. These alloying elements disrupt the continuity of the oxide layer, facilitating a more uniform and sustained dissolution of aluminum. Alloying also enhances operational stability of aluminum, permitting a broader range of electrochemical potentials and pH conditions in Al-air batteries. However, traditional models, such as potential distribution simulations, are constrained by certain assumptions, primarily the neglect of temperature, concentration and reaction kinetics. While PD effectively predict oxidation states and species stability, they do not account for dynamic processes such as electrode degradation or material loss over time. Recent advancements in computational and experimental techniques aim to develop more accurate and comprehensive PD models with Finite element models (FEM). These enhanced models will be crucial in improving the long-term performance and reliability of Al-air batteries, particularly through more sophisticated FEM simulations that consider dynamic, time-dependent processes such as electrode corrosion and degradation. FEM has emerged as a powerful tool for addressing corrosion-related challenges in many inorganic electrodes. It facilitates the simulation of localized corrosion phenomena in aluminum or its alloys by incorporating factors such as alloy microstructure, electrolyte transport properties and electrochemical reaction kinetics. By simulating these dynamic processes, FEM can map anode thinning and corrosion rates, providing insights into how aluminum alloy materials and electrolyte formulations spatially affect battery performances.

Corrosion rates of the materials are modeled by incorporating factors such as electrode morphology, stability of electrode–electrolyte interface, electrolyte concentration and thermodynamic conditions. Electrochemical corrosion of battery electrodes induces both electrode thinning and electrolyte decomposition [21-23]. Assessing these corrosion failures in complete aluminum–air battery stacks is both time-consuming and experimentally demanding. Further, extended exposure to corrosive environments accelerates aluminum dissolution, thereby destabilizing cell performance. Although empirical and mechanistic models provide insights into corrosion, they lack a comprehensive and systematic approach. Constructing PD for aluminium under specific conditions can facilitate the evaluation of redox reactions, corrosion currents, and stable anions/oxides. Traditional PD, developed for metals such as iron and copper, often overlook the presence of protective oxide films, thereby limiting their

predictive accuracy. A refined approach to PD construction, which incorporates the role of protective oxide films, is necessary to more accurately predict and mitigate corrosion effects, ultimately enhancing the durability and performance of aluminum–air batteries.

Electrochemical corrosion of aluminum and its alloys

Electrochemical corrosion of aluminum and its alloys exerts a significant impact on the durability and performance of aluminum-based systems, notably Al-air batteries, by causing electrode thinning and electrolyte decomposition [2-23]. Although extensive research has been conducted on PD for iron and copper (Tables 1 and 2), data concerning aluminum, particularly under non-standard conditions, remain scarce. FEM has been effectively employed to model metal corrosion using thermodynamic data from PD of iron and magnesium [3]. However, a comprehensive understanding of aluminum's corrosion behavior, especially in chloride-rich environments, is still deficient. This knowledge is essential not only for battery electrodes but also for applications such as speedboat hulls, which are frequently constructed from aluminum alloys.

This study aims to develop a comprehensive framework that combines PD generation and FEM to model the corrosion behavior of aluminum and its alloys in Al-air batteries. The novelty of the approach lies in modeling the thickness change of aluminum and its alloys during the corrosion process using both PD and FEM, thereby providing a more integrated and accurate understanding of corrosion phenomena in these systems.

Table 1: E_{corr} values reported in literature.

Refs.	Ecorr /V	Conditions	Pourbaix parameters	I_{corr}/A/cm^2
[9]	−0.7-−0.8	Acidic	pH 0–14 oxide/hydroxide	High-not reported
[12]	−0.8	Aqueous passivity	pH 4–7, passive layer	Very low (10^{-9})
[13]	~−0.9	pH 7, aqueous alloys	pH 7, stable oxide	Moderate (10^{-6})
[14]	−1.1	Alkaline, Al batteries	Alkaline pH, oxide	Very low (10^{-9})
[15]	−0.85	CO_2-rich, Al batteries	CO_2, pH < 7	High (10^{-4})
[15]	−0.85-−1.2	High CO_2, aqueous corrosion	High CO_2, pH ~ 7–8	High (10^{-4})
[16]	−0.5	Neutral to acidic, Al ion batteries	pH 4–7, passive oxide	Very low (10^{-9})
[17]	−1.0	Alkaline electrolytes, Al batteries	Alkaline pH, oxide	Very low (10^{-9})
[18]	~−0.8	Neutral pH corrosion	pH 7, oxide stability	Very low (10^{-9})
[16]	−0.95	Alkaline pH, Al batteries	pH > 9, oxide breakdown	Moderate (10^{-6})
[19]	−0.85	Neutral to acidic, Al ion batteries	pH 4–6, oxide stability	Moderate (10^{-6})
[20]	−1.0	CO_2-rich, Al batteries	High CO_2, pH ~ 7	High (10^{-4})
[17]	−0.9	Alkaline solutions, battery corrosion	pH > 9, oxide stability	Very low (10^{-9})
[20]	−0.95	CO_2-rich, aqueous Al–air corrosion	CO_2, pH ~ 7	High (10^{-4})

The specific goals were to develop empirical models for PD and model thermodynamic behavior of aluminum and its alloys by analyzing: the effect of increased temperature within a corrosion cell on the stability of aluminum species; the influence of varying electrolyte concentrations on aluminum and alloy corrosion; and the impact of changes

in the partial pressure of gases evolved during electrochemical reactions on the accuracy and applicability of PD.

FEM of aluminum corrosion process includes simulating corrosion rates under diverse environmental and operating conditions and predicting thickness variation of aluminum and its alloys as a function of corrosion progression, providing insight into long-term material degradation.

Table 2: Pourbaix method [21-29] and design consideration in developing PD for Al and alloys at various conditions [1-5, 8].

Modern Pourbaix method				
	Advantages	**Disadvantages**	**Performance indicators**	**Ranking**
[25]	Focuses on surface stability	Limited to specific reactions	Good for specific reactions	6
[26]	Combines *ab initio* and experimental data	Requires accurate experimental data	High accuracy for oxide formation	9
MP PBE	Large material database	Inaccurate for transition metal oxides	Broad predictions, lacks precision	4
MP SCAN	Improved accuracy for transition metals	Computationally expensive	More accurate for corrosion and stability	8
Design considerations obtained based on literature				
Category		**Description**	**Equation**	
Equilibrium expressions		PD for Al constructed by combining equilibrium expressions involving Al, $Al(OH)_3$, AlOOH and Al_2O_3	-	
Free energy calculations		Free energy calculations based on chemical potentials of Al species, considering pH and electrode potential	$\Delta G = \Delta G° + RT \ln(Q)$	
Nernst equation		Used to calculate equilibrium potential for reactions involving Al ions and electrons	$E = E° - (RT/nF) \ln(Q)$	
pH-dependent reactions		Influence formation and dissolution of Al_2O_3 and $Al(O)_3$, affecting stability of Al in aqueous solutions	$Al^{3+} + 3H_2O$ □ $Al(OH)_3 + 3H^+$	
Corrosion behavior		Al exhibits passivity due to the formation of a protective oxide layer (Al_2O_3), significantly reducing corrosion	$Al + 3H_2O \rightarrow Al_2O_3 + 6H^+ + 6e^-$	

Developing empirical models for PD

The algorithm to construct a PD for metal under different operating conditions in the empirical model is shown in Fig. 1. At the Al(alloy)-Pt electrode surface node interface, the dissolution of the Al, i.e., electrode reactions, occurs in a fully immersed electrolyte. Al-air corrosion cell typically consists of aluminum or aluminum alloy anode, platinum cathode, and reference electrode made of either platinum or carbon. The cell is immersed in an either alkaline or acidic electrolyte, usually potassium hydroxide, which facilitates ionic conduction and supports electrochemical reactions. At the anode, aluminum undergoes oxidation, releasing electrons and forming Al^{3+} ions (Eq. (1)). These electrons

travel through an external circuit to the cathode, where oxygen reduction occurs, and produce hydroxide ions. The reference electrode, while sometimes a true reference like Ag/AgCl in precise setups, may be a platinum or carbon electrode in simplified systems to monitor the anode potential. This configuration allows for the analysis of aluminum corrosion behavior, including dissolution rates and passivation effects, under controlled electrochemical conditions. Platinum is assumed to be immune to corrosion and helps complete electrochemistry at internal boundaries of Al-Pt-electrolyte domains [29-33]. Aluminum oxidation occurred at the anode and led to its corrosion at -1.676 V. Anodic half-cell reaction considered is given in Eq. (1).

$$Al \leftrightarrow Al^{3+} + 3e^{-} \quad (1)$$

At the cathode, reduction reaction occurs at 1.20 V *vs.* standard hydrogen electrode (SHE). Platinum electrode was used to read the potential of galvanic corrosion in the cell.

$$Pt^{2+} + 3e^{-} \leftrightarrow Pt \quad (2)$$

Thereby, electromotive force of the cell is determined by standard potential difference between cathode and anode in an overall all reaction given below. To benchmark Al corrosion, Evans diagram shown in Fig. 1 was adopted from literature.

$$Al + Pt^{2+} \leftrightarrow Al^{3+} + Pt + e^{-} \; E = 2.876 \text{ V} \quad (3)$$

Accuracy of PD predictions is highly contingent upon the choice of functional. Strongly Constrained and Appropriately Normed functional surpasses Perdew–Burke–Ernzerhof one in terms of precision, particularly when modeling transition metal oxides. This precision is crucial for generating reliable insights into various electrochemical species, rendering the correct functional choice critical for the development of more efficient battery technologies. Designing PD for aluminum necessitates an understanding of oxidation processes, surface chemistry, electrochemical potentials and behavior of oxide layers. The initial step involves constructing a potential-pH diagram, taking into account variations in concentration, temperature and oxide formation. Key regions for oxidation, reduction, corrosion, dissolution and passivity must be identified, with particular attention to alloys and coated metals. The subsequent phase involves refining PD models by incorporating factors such as temperature, pressure and experimental validation to enhance the accuracy of predictions for Al-air batteries. Additionally, integrating Butler–Volmer and Nernst equations is essential for refining corrosion potential, particularly in regions where Gibbs free energy deviates.

Developing FEM for Al corrosion process

Under steady state conditions, potential distribution within electrode–electrolyte of a galvanic system is decisively governed by charge conservation equation, expressed as

$\nabla i = 0$, where i represents current density. According to Ohm's Law, current density is intrinsically linked to the electric field through the equation $i = \sigma E$, with σ being electrical conductivity of the electrolyte. Furthermore, the electric field is related to electrochemical potential (φ) by $E = -\nabla\varphi$. Consequently, the governing equation for potential distribution within the electrolyte is succinctly defined as Laplace's equation (for constant conductivity): $\nabla^2\varphi = 0$. At the interface between electrode and electrolyte, both anodic and cathodic reactions occur simultaneously, resulting in a current density that emerges from electronic exchanges of both processes. In a galvanic couple, cathodic process firmly dominates in the more noble metal (cathode), while anodic process prevails in less noble metal (anode). Butler–Volmer equation unequivocally describes total current density at any electrode–electrolyte interface*:*

$$i_{net} = i_{anodic} + i_{cathodic} = i_0 \exp\left(\frac{a_{anodic}\, zF(\varphi-\varphi_0)}{RT}\right) - i_0 \exp\left(\frac{-a_{cathodic}\, zF(\varphi-\varphi_0)}{RT}\right) \quad (4)$$

In this equation, i_0 denotes exchange current density, while i_{anodic} and $i_{cathodic}$ are critical transfer coefficients for anodic and cathodic reactions, respectively. Additionally, φ_0 signifies equilibrium electrode potential, Z is number of electrons involved in the reaction, F stands for Faraday's constant, R is gas constant and T represents temperature. It is essential to understand that current density at the electrode surface is directly proportional to the normal component of electrochemical potential gradient at the interface.

$$\frac{\partial\Phi}{\partial n} = \frac{i_{net}}{\sigma} \quad (5)$$

Methodology

Overall algorithm for PD for any metals is given in Fig. 1. General outline on the workflow is given in Fig. 2.

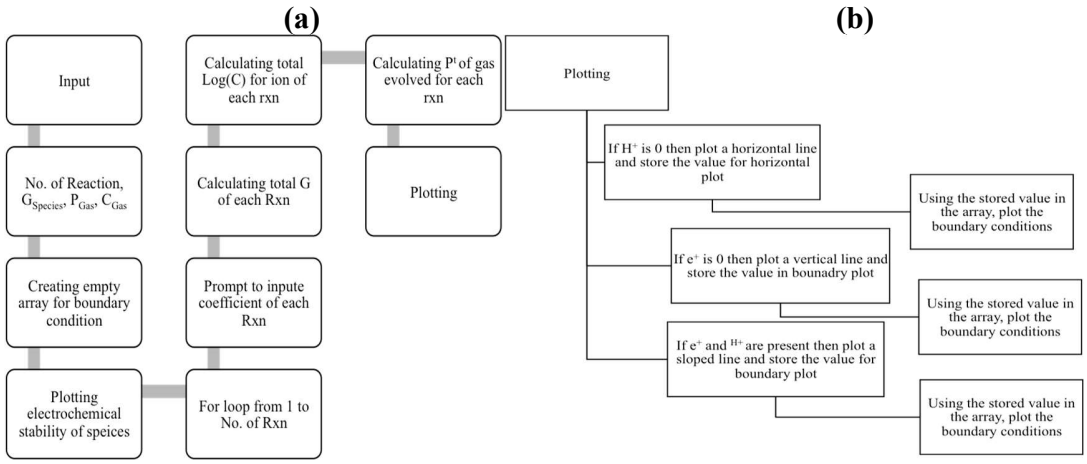

Figure 1: Algorithm for PD for metals. Two different stream block diagrams are presented to understand **(a)** overall approach and **(b)** plotting methods adopted in this study.

Figure 2: Workflow block diagram of the objectives.

Formulating empirical models for PD

Before FEM was devised, Pourbaix diagram was herein constructed using MATLAB v2020a. The code was used as basic framework for constructing PD for aluminum, and results are validated with experimental data. The methodology for constructing PD for aluminum alloys began with identifying relevant species, which included primary alloying elements such as iron, magnesium and zinc, as well as their oxidation states. Solid phases like aluminum, aluminum oxide and aluminum hydroxide, along with aqueous species such as Al^{3+} and AlO_2^-, were considered. Next, relevant equilibrium reactions were formulated, encompassing electron transfer processes, including oxidation and reduction, as well as proton transfer through acid–base interactions, along with redox reactions illustrating both transfers. Comprehensive thermodynamic data were then gathered for each species, including standard reduction potentials, Gibbs free energies of formation and solubility product constants were all sourced from reliable databases and literature to ensure accuracy. Nernst equation was utilized to calculate equilibrium potentials for each redox reaction, considering pH and activities the involved species. These calculated potentials were subsequently plotted on a potential-pH diagram, where each line delineated stability regions for different species, indicating conditions under which they were thermodynamically favoured. An analysis of equilibrium lines enabled identifying stable phases in various regions while considering factors such as pH, potential and the way alloying elements influenced stability and corrosion resistance. To enhance PD robustness, predicted stability regions were validated against experimental data from corrosion potential measurements. Additionally, factors like temperature and complexation reactions were considered for their potential impacts on equilibrium and stability within PD. This streamlined methodology facilitated a comprehensive understanding of the corrosion behavior of aluminum alloys, proving invaluable for their application across diverse environments.

Solving FEM for Al corrosion process

Fig. 3 was used as model geometry to predict aluminum corrosion. The node was used to construct the actual substrate domain in geometry. Both mesh size and solver time were iteratively reduced during repeated geometry simulation. This approach could mimic existing corrosion processes occurring on the metal sheets. Eectrolyte potential and degree of freedom are defined by its boundaries upon determining node size in geometry. To assess material loss, the movement of electrons in the circuit must be monitored in potential or current. Therefore, primary and secondary current distribution

of both interfaces must be found through simulation. Direct current distribution shows how charged ions are transported in an electrolyte. Because current distribution in electrodes is governed by both Ohm's law and charge balance equations, corrosion cell polarization data [26, 27] were required to extract exchange current densities of electrode reactions. Dimensions constructed in FEM and the parameter used in the model for simulation of Al/Pt [36] and Al 7075/Pt [30, 31] are given in Table 3. Governing equations for mass transport, charge conservation and potential distribution were formulated and solved using FEM techniques. PD was integrated into the model by using its predictions of thermodynamically stable phases and corrosion potentials as boundary conditions. For solving FEM equation, a non-linear Neumann boundary condition for Laplace's equation was required, assuming negligible current density at all other domain boundaries. Coefficient form PDE module of COMSOL Metaphysics v5.6 was used for model calibration and validation, recreating two-dimensional geometry based on references [33-35] with default triangular quadratic elements and a normal mesh being required to perform mesh-insensitive result. Potential distributions in the electrolyte were determined by applying Butler–Volmer equations for current densities at the electrode surfaces. Current density at the electrode–electrolyte interfaces was calculated and aluminum corrosion rate at the electrolyte environment was calculated using Faraday's law, ($v = i/zF$), with calculations being focused solely on the anodic surface as only anode corrodes.

Closure equations were created to simulate the effects of applied electrode polarization by providing zero-flux condition on upper boundary Dirichlet condition at fixed potential. The impact of varying electrode orientations was explored through the modeling of two non-coplanar electrodes. Secondary current distribution interface accounted for overpotential in the cell. Both charge transfer and overpotential were used as an arbitrary kinetic expression. Butler–Volmer and Tafel equations were employed to calculate material loss by corrosion. Using secondary current distribution data, exchange current density of cathodic and anodic polarization was obtained. Furthermore, the model required material properties such as elastic modulus yield strength and corrosion resistance for analyzing corrosion behavior in a 2D structure. Iterations of simulations were then conducted to predict corrosion pit growth, stress and strain distribution, and remaining service life. In electrode corrosion simulations, the electrolyte potential distribution was resolved by applying boundary conditions that represented interfaces: current fluxes for anodic and cathodic surfaces derived from polarization data and zero-flux conditions for symmetry boundaries. Accurate representation of steep potential and current gradients requiresd a carefully designed computational grid. A non-uniform mesh was typically employed, with fine elements (on the order of 10^{-5}–10^{-4} m) concentrated near metal–electrolyte interfaces, crevices and galvanic junctions, where electrochemical reactions were most intense. The mesh

was progressively coarsened in bulk electrolyte, where gradients diminished, to optimize computational efficiency. Grid independence was verified by systematic refinement until computed potentials and current densities varied by less than 1-2% between successive mesh levels. Tetrahedral elements are commonly used in three-dimensional domains, with aspect ratios kept below five to preserve numerical stability. COMSOL enable finer control of grid topology, adaptive refinement and more accurate coupling of electrochemical processes.

Experimental data collection

Fig. 3 portrays the experimental setup adopted in this study. On the left side, a there is modified schematic of the corrosion cell, which was used to measure all polarization curves. A metal sample was mounted in the epoxy pick and placed in the cell.

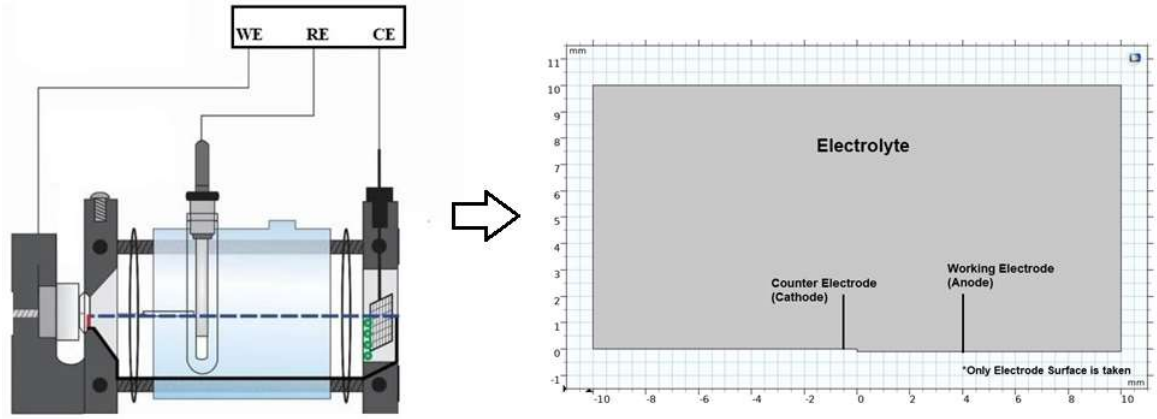

Figure 3: Experimental apparatus used for data collection [25] and FEM.

The figure shows that the reference electrode (SHE) and counter electrode (platinum) were positioned in the capillary tube. The metal substrate acted as working electrode was placed in an optimized location to minimize IR drop. Exact dimensions of the cell and boundary angles employed in experimental setup were selected to create the model's cell geometry (Table 3). The electrodes were thoroughly cleaned utilizing an ultrasonic bath with acetone and isopropanol, followed by activation in a 0.5 M H_2SO_4 solution through cyclic voltammetry. To maintain a stable acidic environment, the electrolyte was precisely prepared by diluting concentrated sulphuric acid with deionized water for achieving a concentration of 1 M electrolyte. Tafel polarization measurements were conducted at a scan rate of 1 mV/s over a potential range from -0.2 to +0.8 V with respect to Ag/AgCl, using a 0.1 M KCl solution as reference electrolyte. All measurements were carried out at room temperature, ensuring that experimental setup was both clear and fully reproducible.

Table 3: Cell details and parameters of both Al and Al alloy used in the model.

Cell details		
Space dimension	**2d**	
Physics	Corrosion study with secondary current distribution	
Working electrode (anode)	Al/al 7075	
Counter electrode (inert cathode)	Pt	
Electrolyte	Seawater with 5 S/m of electrolyte conductivity	
Time	0 to 48 h (2 days)	
Deforming electrode	Al or Al alloy anode	
Non-deforming boundary	Rest of the boundary, including the cathode	
Al electrode details		
Electrode height	10 mm	
Cathodic electrode surface	10 mm in length + 0.1 mm edge	
Anodic electrode surface	10 mm in length	
Electrolyte area	201 mm^2	
Parameters of Al		
Name	Description	Value
E0al	Equilibrium potential for Al	-1.676 V
E0pt	Equilibrium potential for Pt	1.2 V
Sigma	Transfer coefficient	5 S/m
Denal	Density of Al	2700 Kg/m^3
Mmal	Molar mass of Al	0.027 Kg/mol
C_{dal}	Anodic current density of Al	10-8.85 A/m^2
Cdpt	Cathodic current density of Pt	2×10^{-3} $A\text{-}m^{-2}$
Sal	Anodic Tafel slope for Al	0.173 V
Spt	Cathodic Tafel slope for Pt	-0.18 V
Parameters of Al 7075		
Name	**Description**	**Value**
E07075	Equilibrium potential for Al 7075	-1.7 V
E0pt	Equilibrium potential for Pt	1.2 V
Sigma	Transfer coefficient	5 S/m
Den7075	Density of Al 7075	2810 kg/m^3
Mm7075	Molar mass of Al 7075	0.0268 kg/mol
S7075	Anodic tafel slope of Al 7075	0.37 V
Cdpt	Cathodic current density of Pt	2×10^{-3} $A\text{-}m^{-2}$
Cdpt	Cathodic current density of Pt	2×10^{-3} $A\text{-}m^{-2}$
Spt	Cathodic Tafel slope for Pt	-0.18 V

Results and discussion

Empirical modelling of PD for aluminum

To account for complex interactions such as concentrations and temperature variations that affect metal performance, first principal approach, which starts from elementary reactions related to Al corrosion, was herein used. Furthermore, stability of Al species in untested conditions was herein explored by assessing deviations in metal performance under highly acidic conditions, such as different species like $AlCl_3$ forming in chloride-rich environments. An empirical model can incorporate this to improve corrosion risk predictions. Governing reactions to construct a PD for Al are:

$$Al^{3+} + 3e^- \leftrightarrow Al \quad (6)$$

$$Al_2O_3 \cdot H_2O + 6H^+ \leftrightarrow 2Al^{3+} + 4H_2O \quad (7)$$

$$Al_2O_3 \cdot H_2O + 6H^+ + 6e^- \leftrightarrow 2Al + 4H_2O \quad (8)$$

$$2AlO^{2-} + 2H^+ \leftrightarrow 2Al_2O_3 \cdot H_2O \quad (9)$$

$$AlO^{2-} + 4H^+ + 3e^- \leftrightarrow Al + 2H_2O \quad (10)$$

As these reactions take place in a half-cell, and the other half-cell is a SHE with 0 V, it was easy to measure overall EMF of the cell. Thermodynamic material data [15] collected and computed based on data provided in ASTM handbook for this work is shown in Table 4.

Table 4: Thermodynamic data obtained from the study.

Species	298 K G^0 (J/mol)	H^0 (J/mol)	S^0 (J/mol*K)	C_p (J/mol*K)	373 K G^0 (J/mol)	423 K G^0 (J/mol)	473 K G^0 (J/mol)
Al	0	0	28.3	24.2	−10,767	−12,532	−14,439
Al^{3+}	−485,000	−531,000	−321.7	−122.65	−409,935	−392,079	−373,497
$Al_2O_3 \cdot H_2O$	−1,831,700	−1,980,700	96.86	131.25	−2,017,975	−2,024,713	−2,032,228
AlO_2	−830,900	−930,900	−33.41	−33.41	−916,882	−914,560	−912,039
H_2O	−228,600	−241,800	188.8	33.6	−312,520	−322,441	−332,565

The reaction was converted to equations in terms of pH and potential using standard Gibbs free energy values.

$$pH = 2.75 - 0.33 \times \log(Al^{3+}) \quad (11)$$

$$E = -1.516 - 0.059 \times pH \quad (12)$$

$$pH = 12.93 + \log(AlO^{2-}) \quad (13)$$

$$E = -2.08 - 0.019 \times [pH - \log(1/AlO^{2-})] \quad (14)$$

PD for aluminum constructed using an empirical modeling basis at standard conditions are shown below in Fig. 4. The red dotted line depicts the region of water stability, and equations regarding electrochemical stability of water are included in the figure. The area where ions are formed represents corrosion, and the location where oxide and hydroxides are formed portrays passivation. Aluminum can be processed at high pressures or temperatures in industries depending on their requirements. Therefore, constructing a PD under different states will be helpful, requiring thermodynamic material data such as standard enthalpy, entropy and molar heat capacity [36–38], as shown in Table 4. Substituting these values provides Gibbs free energy at 373, 423 and 473 K, as shown in the table. Plots (Figs. 4 and 5) related to solid or low-level corrosion attacks are provided.

Constructing a PD depends on the thermodynamic stability of aluminum in aqueous or alkaline environments, illustrating the stable phases of Al or its alloys based on the electrode potential. Equilibrium lines for different oxidation states were herein

plotted, with enclosed regions indicating stable phases under specific conditions being used as a preliminary metric for modeling dissolution and degradation behavior of Al or its alloys. However, they have limitations, such as not accounting for kinetic factors like reaction rates and overlooking variables such as temperature, pressure and complex ion interactions. Despite these drawbacks, PD could remain invaluable for understanding electrochemical behavior and directing research across multiple disciplines.

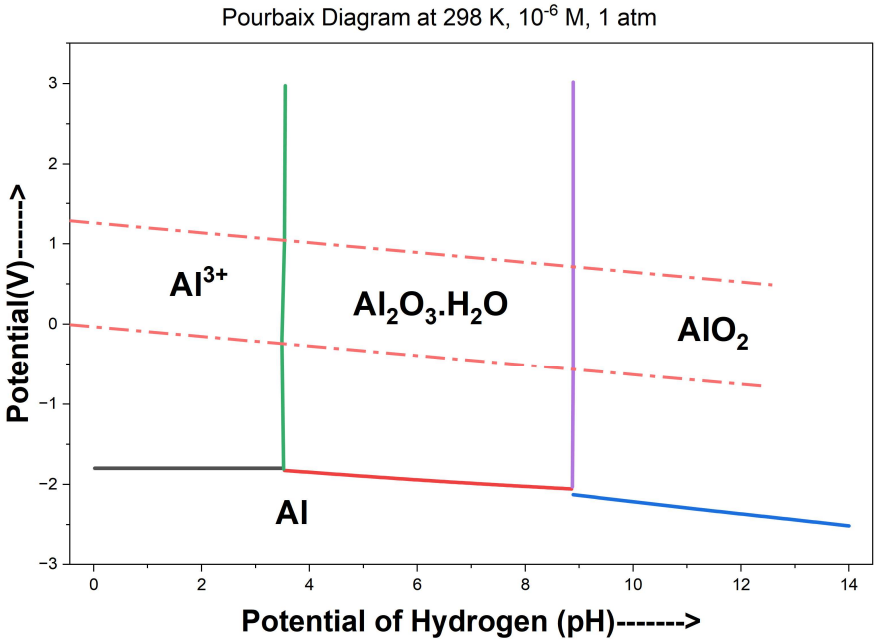

Figure 4: PD for aluminium at 298 K and 10^{-6} M (baseline). Color differences show the boundary amongst each species. Dotted lines reflect baseline samples.

When temperature increased, the shape of the PD also changed (Figs. 4 and 5). Immunity region slightly expanded as there was a change in potential of the horizontal line, due to the increase in kinetic energy of the particle, which further increased rate of collision. In the region of water stability, corrosion region of Al to Al^{3+} and passivation region of $Al_2O_3 \cdot H_2O$ reduced, because temperature accelerated anodic reaction and further increased passive current density. This resulted in narrowing of the inactive part in heated solutions, and metal passivation became challenging. Corrosion region of Al to AlO^2 significantly enlarged with the increase in temperature. Thus, it was better to use Al at low temperatures to increase resistance and passivation. When the ion concentration increased from 10^{-6} to 0.01, immunity region of Al remained the same (Figs. 4 and 6). Corrosion region of Al^{3+} and AlO^{2-} reduced slowly, but passivation region of $Al_2O_3 \cdot H_2O$ increased drastically, since the higher concentration of ions in the electrolyte increased the possibility of Al reacting with

oxygen, forming a passive region [31-33]. Hence, it was good to have Al with a higher concentration of ions in the electrolyte to prevent its corrosion.

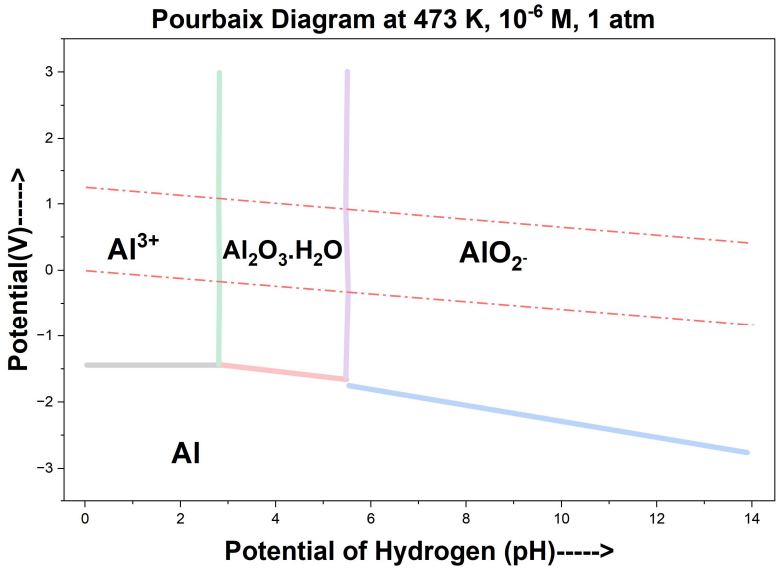

Figure 5: PD for aluminium at 473 K. Color differences shows the boundary amongst each species.

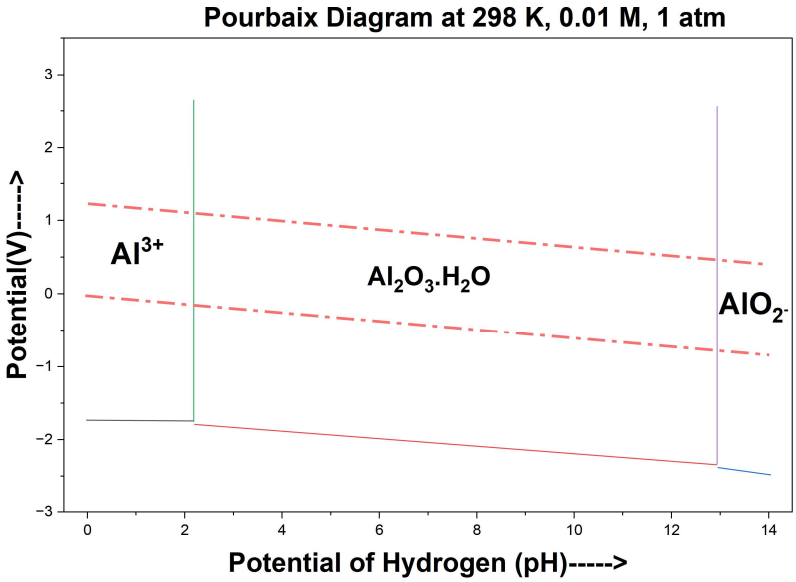

Figure 6. PD for aluminium at 298 K and 1 × 10^{-2} M.

Figs. 4 and 7 demonstrate that, as partial pressure of gas in the electrochemical reaction increased, there was not much change in Pourbaix diagram's shape, because the reaction has no gas phase at 25 °C, and the graph may change when temperature rises

to 100 °C. Generally, Al and its alloy 7075 are highly corrosion-resistant in the environment. Al has a high affinity for oxygen, and it reacts with atmospheric oxygen, forming a porous passive layer on top of the metal surface. In the case of Al 7075, 90% Al reacts with oxygen to create a passive layer, but the remaining percent of elements in the alloy, like iron, copper and magnesium, react with O_2 to form rust that does not passivate. In this study, Al and its alloy 7075 were immersed in seawater with 3.5 weight % NaCl electrolyte. These chloride ions pass through the porous metal oxide layer to react with Al, thus leading to corrosion. Al 7075 is more anodic than pure Al, as more intergranular metals are present in the alloy. So, they suffer more corrosion than Al. Thus, it was evident from Figs. 6b and 8a that Al 7075 geometry had a more corroded area and corrosion rate than Al under the same electrolytic conditions.

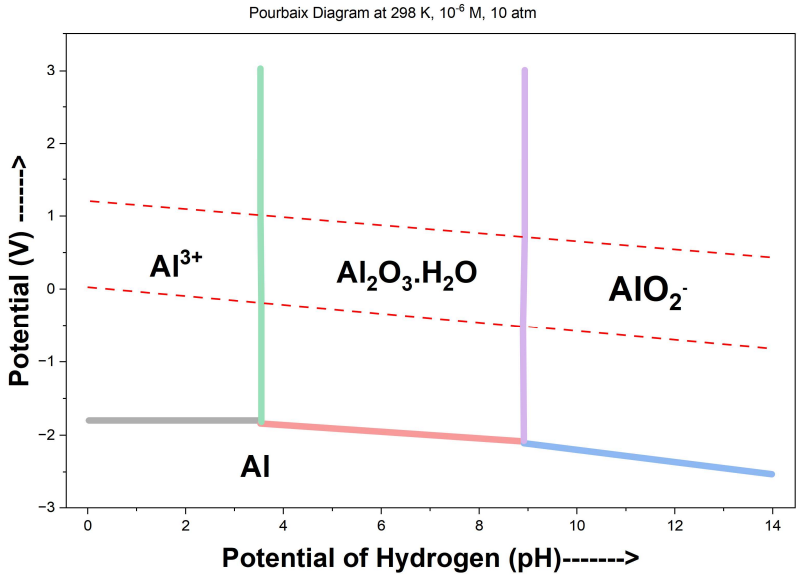

Figure 7: PD for Al at 298 K and10 atm.

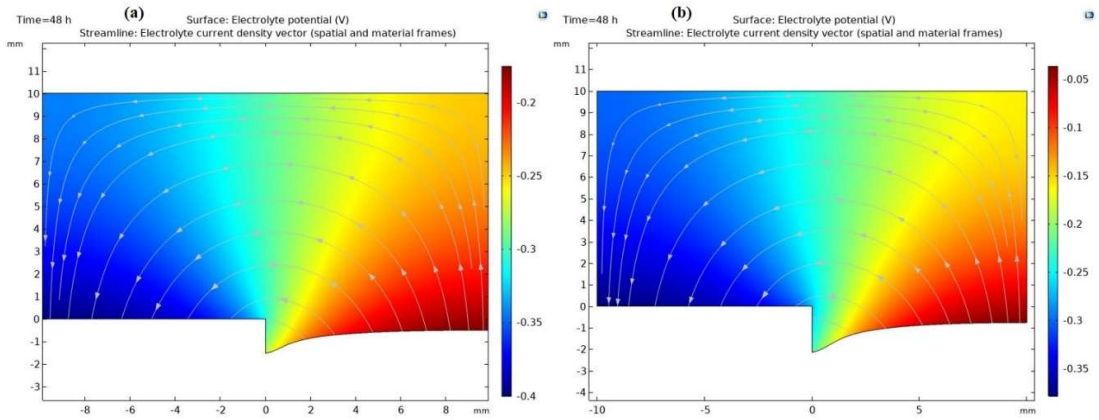

Figure 8: Deformed geometry of (**a**) Al (baseline) and (**b**) Al 7075.

Corrosion of Al 7075 was stronger than that from pure Al, with the corroded depth at the anode being greater for Al 7075. As shown in Fig. 8, the anode of pure Al eroded to form a pit with a depth of 1.31 mm at overpotential of 1.93 V, while Al 7075 eroded to a pit of 1.9 mm at 1.87 V, with a larger corroded area. The study, based on PD and two-dimensional FEM, indicates that potential difference between Pt and Al/Al alloys in the electrolyte generated an electron flow, causing Al alloy to corrode due to its more negative potential. Electrochemical potential difference between the materials drives galvanic corrosion. PD and polarization diagrams illustrate current distribution on the metal surface. While Al is corrosion-resistant and passivate in oxidizing conditions, it releases corrosion products due to its sacrificial nature. Corrosion potential and current for Al and its alloys were estimated graphically and analytically, with current exchange densities for hydrogen evolution extracted from Tafel plots. Localized attacks on the alloys, predicted by secondary current distribution and material loss, may result in pit formation. Small destructive pits could deepen and cause further weight loss. Severity of pitting corrosion was found to be dependent on pH, temperature and concentration, with pitting correlating to chloride ion presence in seawater, like other studies. Further analysis of pitting and its correlation with potential is needed to aid in alloy development and failure analysis.

Fig. 9 highlights electric current flowing per unit cross-sectional area of both electrolyte and electrode surface, with the current density being indicative of reaction current density. To quantitatively evaluate corrosion behavior, both Al and Al 7075 specimens underwent standardized corrosion testing following ASTM, involving immersion in a 3.5% NaCl electrolyte solution under controlled conditions. Critical parameters, including weight loss, corrosion depth and electrochemical behavior, were meticulously measured, revealing corrosion percentages of 13.1% for pure Al and 19% for Al 7075 over a 2-day immersion period. These findings compellingly indicate that Al 7075 has a significantly higher corrosion rate than pure Al. Traditional PD present a limited view, as they do not offer insights into electrochemical reaction rates the time-dependent behaviours of various species. Instead, these diagrams illustrate thermodynamic stability of electro active species across a range of pH levels and potential conditions.

To overcome these shortcomings, it is essential to develop a specialized FEM that incorporates kinetic factors using Butler–Volmer equations. Further, the graph compares overpotential and thickness variation of two materials: Al and Al 7075. Overpotential represents the extra voltage required beyond theoretical voltage for electrochemical reactions, such as corrosion or hydrogen evolution, and higher values indicate less efficient performance, which is critical to recognize. Thickness variation refers to changes in material's thickness due to corrosion or electrochemical degradation, and the graph effectively illustrates how of Al and Al 7075 thickness changed as overpotential increased. Notably, the relationship between overpotential

and thickness variation for aluminum shows that a significant increase in overpotential with minor thickness changes suggests rapid degradation or passivation. In contrast, Al 7075 exhibits distinct electrochemical behavior; the plot clearly demonstrates how the alloy's corrosion resistance or performance diverges, indicating either a more stable or variable overpotential with thickness change.

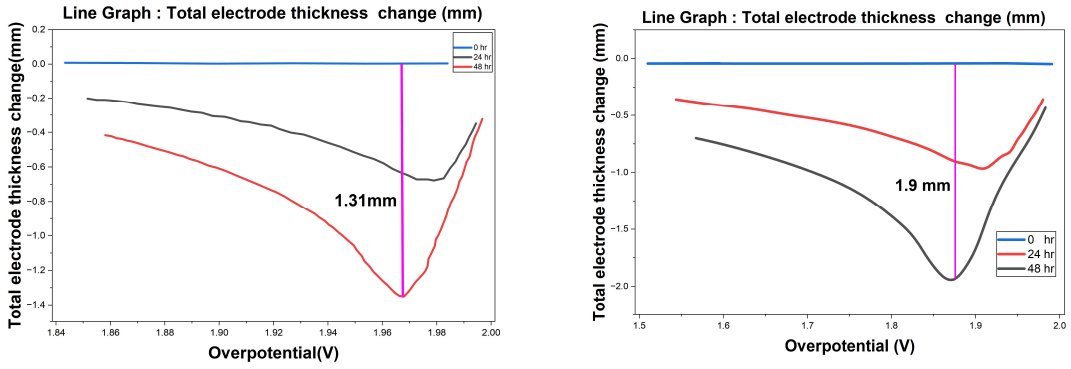

(**a**) (**b**)

Figure 9: Overpotential and thickness variation of (**a**) Al (baseline), and (**b**) Al 7075, respectively**.**

The combined use of PD and FEM offers a comprehensive approach to designing Al and Al alloy electrodes for Al-air batteries. PD help identify stable electrochemical regions and corrosion tendencies, but are limited in addressing thickness effects and complex alloy behavior. FEM complements them by simulating current distribution, phase behavior and localized corrosion under varied conditions, making it valuable for optimizing electrode geometry and composition. Al alloys outperform pure Al in stability and conductivity, and FEM effectively captures how thickness and material variations influence performance. While PD aid in material screening, FEM supports real-world design, making the integration of both methods essential for developing efficient, durable electrodes.

Accurately modeling the thickness of the electrode–electrolyte interface is essential for comprehending its influence on charge transfer resistance, local pH gradients and Al dissolution rates during discharge cycles of batteries. A thinner interface, as demonstrated through spatial mapping of the electrode, can reduce charge transfer resistance, thereby enhancing battery efficiency. However, this reduction may also exacerbate local pH gradients, leading to accelerated Al dissolution and corrosion. Over successive discharge cycles, this increased dissolution can result in structural degradation of the electrode material, ultimately reducing the battery's lifespan. From a thermodynamic standpoint, thicker interfaces tend to stabilize the local environment,

potentially mitigating corrosion but possibly limiting the rate of charge transfer, thus affecting overall battery performance. Achieving an optimal balance between interface thickness, charge transfer resistance and dissolution rates is critical for enhancing both efficiency and longevity of Al-air batteries.

Benefits and limitations of the modelling framework

The advanced framework presents several notable advantages for simulation and comprehension of electrochemical systems. Benefits and constraints are listed out in Table 5.

Benefits

By characterizing current density as a function of overpotential for both anodic and cathodic reactions, it facilitates the simulation of transient electrochemical responses, which is essential for examining reaction rate limitations. This capability is particularly significant in applications such as charging and discharging cycles, where dynamics may evolve over time. The capacity of the model to incorporate electrochemical degradation processes addresses a critical shortcoming of traditional PD, especially in the design of metal–air batteries. It provides a more precise depiction of electrode losses, a prevalent issue in systems like Al-air batteries, where corrosion poses challenges. Furthermore, the model captures crucial information such as stress corrosion distributions and localized current density contours that contribute to material degradation. This approach integrates thermodynamic stability with extensive kinetic processes and degradation mechanisms, offering a dynamic and realistic representation of electrochemical systems. By incorporating time-dependent behavior and accounting for material decay rate, the model offers insights into the structural integrity and long-term performance of electrochemical systems, rendering it invaluable for applications where durability is a critical consideration.

Limitations

Despite its advanced capabilities, the modeling framework possesses certain limitations that warrant consideration. One challenge is the complexity involved in accurately modeling time-dependent electrochemical behaviours and degradation processes. This necessitates meticulous attention to electrode kinetics at the electrode-electrolyte interface, which can increase computational complexity and potentially limit the model's scalability. Additionally, while the model captures the effects of material loss and corrosion, it may not fully account for all physical phenomena involved in electrochemical degradation, such as complex microstructural changes or interactions with varying environmental conditions. Although the framework provides a detailed representation of corrosion processes, its accuracy in predicting long-term material performance might still be influenced by uncertainties in input

parameters, material properties and boundary conditions. The necessity for high-fidelity experimental validation is critical, particularly when applying the model to real-world systems with complex and variable conditions, such as marine environments where aluminum alloys are exposed to diverse corrosive agents. Thus, while the model represents a significant advancement, further refinements and validations are necessary for it to achieve widespread application in industrial contexts. A comparison between Al and Al alloy tested in the proposed framework is displayed in Table 5.

Table 5: General benefits of the framework.

Aspect	Al	Al Alloys	Pourbaix diagram inference	FEM inference
Performance	Moderate	High but as electrode degradation would be higher	Shows stable zones; lacks thickness/performance detail	Models thickness and current flow for optimized design
Corrosion resistance	Moderate; prone to attack	Varies; often better	Predicts corrosion zones in pH vs. potential	Simulates localized corrosion under varied thickness
Electrochemical stability	Stable in pH 6–9	Broader pH range	Maps stability regions	Captures dynamic stability with time/pH changes
Phase behaviour	Forms Al_2O_3 layer	Alloy-specific phases	Shows oxide formation; limited to pure Al	Models multi-phase behaviour in thicker alloy electrodes
Design optimization	Limited flexibility	Customizable	Not suited for design modelling	Simulates shape/thickness impact on current distribution
Alloy composition evaluation	Simple	Complex, tuneable	Shows base metal trends	Evaluates performance by simulating alloy variations
Material stability	Susceptible to pitting	Generally more stable	Highlights thermodynamic stability	Predicts degradation based on geometry and composition
Corrosion mechanism	General and localized	Localized, galvanic possible	Does not model mechanisms	Simulates detailed corrosion processes
Thickness variation impact	Limited impact	Significant; design-dependent	Not captured	Key for performance tuning and failure prediction

Conclusions

In conclusion, data-driven analysis conducted in this study provides compelling evidence of the significant impact of galvanic corrosion on aluminum and its alloys in alkaline and acidic electrolyte environments. FEM, validated by experimental data, reveals a clear correlation between immersion time and rate of material loss for both pure Al and Al 7075. Specifically, corrosion testing indicated a weight loss of 13.1%

for pure Al and 19% for Al 7075, after a 2-day immersion period in an electrolyte solution, demonstrating that Al 7075 is more susceptible to corrosion than pure Al.
These findings were further corroborated by mathematical modeling measurements of corrosion depth, with pure Al exhibiting a maximum pit depth of 1.31 mm at an overpotential of 1.93 V, compared to a deeper 1.9 mm pit at 1.87 V for Al 7075. FME simulations also captured localized effects of corrosion, particularly around defects in the oxide layer, where even minor disruptions led to significant changes in corrosion current. This aligns with experimental observations, indicating that corrosion behavior is influenced not only by alloy composition but also by surface conditions and the presence of localized defects.
Feedback loop in aluminum corrosion in Al-air batteries degradation was also quantitatively evaluated, revealing an increase in corrosion rates at the waterline, further exacerbated by the electrochemical interaction between submerged aluminum surfaces and seawater.
Collectively, the data underscore the necessity of implementing targeted design metrics to overcome corrosion in battery environment, such as alloying the anodes or advanced alloy making protocols, to mitigate accelerated corrosion rates and maintain Al-based electrodes integrity.
The distinct differential corrosion behavior between pure Al and Al 7075 highlights the need for tailored protective solutions depending on alloy choice and application, ensuring the longevity of Al-based structures in demanding marine environments.

Funding
This research received no external funding.

Data availability statement
The original contributions presented in the study are included in the article; further inquiries can be directed to the corresponding author.

Authors' contributions
S. R. Dhanushkodi: data modeling, analysis and verification; Software; theoretical analysis; paper draft writing. **S. Sangeetha**: data analysis and verification; Software; theoretical analysis. **M. N. Babu**: paper draft writing. **M. W. Fowler**: revisions; project management.

Acknowledgments
All authors wish to express their gratitude and congratulate Professor Mark David Pritzker, University of Waterloo, for his inspiring career on electrochemistry and contribution to PD developed in his research. The contributions from capstone students Mr. Balaji and Mr. Naveen are duly acknowledged.

Conflicts of interest

The authors declare no conflict of interest.

Abbreviations

Al: aluminum
Al2O$_3$: aluminum oxide
Al$_3^+$: aluminum ion
Al-air: aluminum-air
AlO$_2^-$: aluminate
CE: counter electrode;
e$^-$: electrons
FEM: finite element model
H$^+$: hydrogen ion
H$_2$O: water
PD: Pourbaix diagram
pH: potential of hydrogen
Pt: platinum
MATLAB: Matrix Laboratory
SHE: standard hydrogen electrode
WE: working electrode

References

1. Liu X, Jiao H, Wang M et al. Current progresses and future prospects on aluminium–air batteries. Intern Mater Rev. 2022;67(7):734-764. https://doi.org/10.1080/09506608.2021.2006968
2. Shabeer Y, Madani SS, Panchal S et al. Different metal–air batteries as range extenders for the electric vehicle market: A comparative study. Batteries. 2025;11(1):35. https://doi.org/10.3390/batteries11010035
3. Wang T, Yang T, Luo D et al. High-energy-density solid-state metal–air batteries: Progress, challenges, and perspectives. Small. 2024;20:2309306. https://doi.org/10.1002/smll.202309306
4. Buckingham R, Asset T, Atanassov P. Al-air batteries: A review of alloys, electrolytes and design. J Pow Sour. 2021;498:229762. https://doi.org/10.1016/j.jpowsour.2021.229762
5. Ashurov I, Iskandarov S, Khalilov U et al. Current challenges, progress and future perspectives of Al-ion batteries. Appl Sol Ener. 2022;58(3):334-354. https://doi.org/10.3103/S0003701X22030033
6. Fontana MG. Corrosion engineering (3rd ed.). McGraw-Hill. 1986.
7. Evans UR. Corrosion and corrosion control: An introduction to Corros Sci and engineering. Wiley-Interscience. 1947.

8. Verink ED. Economics of corrosion. In R. W. Revie (Ed.), Uhlig's corrosion handbook. 2011, pp. 11–25. John Wiley & Sons.
9. Pourbaix M. Atlas of electrochemical equilibria in aqueous solutions. NACE. 1974.
10. Cook W, Olive R. Pourbaix Diagrams for the iron-water system extended to high-subcritical and low-supercritical conditions. Corros Sci. 2012;58:326-331. https://doi.org/10.1016/j.corsci.2011.10.034
11. Perry SC, Gateman SM, Stephens LI et al. Pourbaix Diagrams as a simple route to first-principles corrosion simulation. J Electrochem Soc. 2019;166:C3186. https://doi.org/10.1149/2.0111911jes
12. Sato N. An overview on the passivity of metals. Corros Sci. 1990;31:1-19. https://doi.org/10.1016/0010-938X(90)90086-K
13. Xu C, Nešić S. Corrosion of Al alloys in aqueous solutions: Electrochemical behavior and corrosion inhibition. Corros Sci. 2011;53;1614-1626. https://doi.org/10.1016/j.corsci.2011.01.003
14. Tan J, Wang D, Cao H et al. Effect of local alkaline microenvironment on the behaviors of bacteria and osteogenic cells. ACS Appl Mater Interf. 2018;10(49):42018-29. https://doi.org/10.1021/acsami.8b15724
15. Zhao Y, Xie J, Zeng G et al. Pourbaix diagram for HP-13Cr stainless steel in the aggressive oilfield environment characterized by high temperature, high CO_2 partial pressure, and high salinity. Electrochim Acta. 2019;293:116-127. https://doi.org/10.1016/j.electacta.2018.08.156
16. Liu Z, Hu Y. Recent progress in inhibition of hydrogen evolution reaction in alkaline Al-air batteries. Nation Sci Op. 2024;3(6):20240037. https://doi.org/10.1360/nso/20240037
17. Burstein GT, Liu C, Souto RM et al. Origin of pitting corrosion. Corros Eng Sci Technol. 2004;39:25-30. https://doi.org/10.1179/147842204225016859
18. Guo L, Huang Y, Ritacca AG et al. Effect of indole-2-carboxylic acid on the self-corrosion and discharge activity of Al alloy anode in alkaline Al–air battery. Molecules. 2023;28(10):4193. https://doi.org/10.3390/molecules28104193
19. Coma M, Puig S, Pous N et al. Biocatalysed sulphate removal in a BES cathode. Biores Technol. 2013;130:218-223. https://doi.org/10.1016/j.biortech.2012.12.050
20. Kim JS, Kim B, Kim H et al. Recent progress on multimetal oxide catalysts for the oxygen evolution reaction. Adv Ener Mater. 2018;8(11):1702774. https://doi.org/10.1002/aenm.201702774
21. Dieudonné T, Marchetti L, Wery M et al. Role of copper and aluminum additions on the hydrogen embrittlement susceptibility of austenitic Fe-Mn-C TWIP steels. Corros Sci. 2014;82:218-226. https://doi.org/10.1016/j.corsci.2014.01.022

22. Wu YH, Lin WJ, Tsai TH et al. Unveiling the reaction mechanism of aluminum and its alloy anode in aqueous Al cells. ACS Appl Ener Mater. 2024;7(9):3957-3967. https://doi.org/10.1021/acsaem.4c00264
23. Pogliani L. Construction and usefulness of the Pourbaix E-pH diagrams. In Chemistry and Industrial Techniques for Chemical Engineers. 2020, (pp. 3–19). Apple Academic Press. https://doi.org/10.1201/9780429286674
24. Tanupabrungsun T, Young D, Brown B et al. Construction and verification of PD for CO_2 corrosion of mild steel valid up to 250 °C. NACE - International Corrosion Conference Series. 2012;4:3329-3344.
25. Hansen HA, Rossmeisl J, Nørskov JK. Universality in oxygen reduction electrocatalysis on metal surfaces. ACS Catal. 2012;2:662-667. https://doi.org/10.1021/cs300227s
26. Persson K, Bengtson A, Ceder G et al. Ab initio study of the composition dependence of the pressure-induced spin transition in the $(M_{g1-x}Fe_x)O$ system. Geophys Res Lett. 2006;33:L16306. https://doi.org/10.1029/2006GL026621
27. Jain A, Ong SP, Hautier G et al. Commentary: The Materials Project: A materials genome approach to accelerating materials innovation. APL Mater. 2013;1;011002. https://doi.org/10.1063/1.4812323
28. Holze R. Electrochemistry: Subvolume—An electrochemical thermodynamics and kinetics. Springer. 2007. https://doi.org/10.1007/978-3-540-41038-6
29. Singh A, Lin Y, Liu W et al. Berberine as an effective corrosion inhibitor for 7075 Al alloy in 3.5% NaCl solution. Intern J Electrochem Sci. 2014;5:5164-5176. https://doi.org/10.1016/S1452-3981(23)08158-0
30. Fontes E. Modelling pitting corrosion in COMSOL Multiphysics. COMSOL. 2021. https://www.comsol.com/blogs/modelling-pitting-corrosion-in-comsol-multiphysics.
31. Olanipekun AT, Oluwabunmi K, Oladosu T. Galvanic corrosion of a mild steel bolt in a magnesium alloy (AZ91D) plate simulation using COMSOL Multiphysics. Intern J Sci Eng Res. 2014;5;1329-1332. https://doi.org/10.13140/R.G.2.2.16630.40006
32. Frankel GS. Pitting corrosion of metals: A review of critical factors. J Electrochem Soc. 1998;145:2186-2198. https://doi.org/10.1149/1.1838615
33. Uhlig HH. The adsorption theory of passivity and the Flade potential. Zeitschr Elektrochem. 1958;62:626-632.